buildings

MDPI

Article

Nonlinear Subharmonic Resonance Instability of an Arch-Type Structure Under a Vertical Base-Excitation

Zilin Zhong [1,2,*], Xiaobin Xu [1], Fulin Shen [1], Zhiyong Yao [1] and Weiguo Xiao [1]

[1] Academician Workstation, Guangzhou Railway Polytechnic, Guangzhou 511300, China; xuxiaobin008@gtxy.edu.cn (X.X.); shenfulin@gtxy.edu.cn (F.S.); yaozhiyong@gtxy.edu.cn (Z.Y.); xiaoweiguo@gtxy.edu.cn (W.X.)
[2] Research Centre for Wind Engineering and Engineering Vibration, Guangzhou University, Guangzhou 510006, China
* Correspondence: zhongzilin@gtxy.edu.cn

Abstract

This study develops an analytical framework for investigating in-plane nonlinear subharmonic resonance in fixed–fixed circular arches under a vertical base-excitation, a phenomenon not adequately addressed in previous research. Based on Hamilton's principle, the governing partial differential equation for in-plane nonlinear motion is first derived. The tangential displacement is then expressed as a modal superposition, and the system is reduced to a set of second-order ordinary differential equations via the Galerkin method. Using the method of multiple scales, the nonlinear 1/2-subharmonic resonance is solved, yielding closed-form, steady-state amplitude–phase relations and corresponding stability conditions. Validation against finite element simulations and Runge–Kutta analyses confirms the accuracy of the proposed approach. Dimensionless fundamental frequencies match finite element results exactly, with discrepancies in critical base-excitation below 2.5%. A close agreement is observed in both the amplitude–frequency and force–response curves with numerical predictions and Bolotin's method, accurately capturing the characteristic hardening nonlinearity and three distinct dynamic regions spanning negligible vibration, stable resonance, and instability. Parametric studies further reveal key trends. Larger included angles intensify the vibration amplitude and promote saddle-node bifurcation, while narrowing stable operating regions. Higher slenderness ratios enhance structural flexibility and nonlinearity, shifting resonant peaks toward higher frequencies. Increased damping suppresses the response amplitude and raises the thresholds for vibration initiation and bifurcation.

Keywords: arch; nonlinear sub-harmonic resonance; dynamic instability; vertical base-excitation

check for updates

Academic Editor: Antonio Formisano

Received: 4 November 2025
Revised: 21 November 2025
Accepted: 27 November 2025
Published: 1 December 2025

Citation: Zhong, Z.; Xu, X.; Shen, F.; Yao, Z.; Xiao, W. Nonlinear Subharmonic Resonance Instability of an Arch-Type Structure Under a Vertical Base-Excitation. *Buildings* **2025**, *15*, 4356. https://doi.org/10.3390/buildings15234356

Copyright: © 2025 by the authors. Licensee MDPI, Basel, Switzerland. This article is an open access article distributed under the terms and conditions of the Creative Commons Attribution (CC BY) license (https://creativecommons.org/licenses/by/4.0/).

1. Introduction

Owing to their efficient mechanical load-bearing capacity, arch-type structures are widely applied in fields such as civil engineering and micro-electromechanical systems (MEMSs), and their dynamic stability is directly related to engineering safety and device reliability. In the field of civil engineering, structures like arch bridges and building roofs often encounter the issue of non-uniform foundation settlement. This phenomenon can cause non-uniform movement or the rotation of supports, thereby significantly altering the in-plane nonlinear instability behavior of arches [1]. Similarly, within MEMSs, shallow arch microbeams subjected to electrostatic excitation may undergo dynamic snap-through

motion and exhibit chaotic attractors, severely compromising device functionality [2]. Furthermore, temperature variations impart a temperature dependence to the mechanical properties of functionally graded material (FGM) arches, consequently influencing their critical buckling loads [3]. Under impact loads, the dynamic buckling load of fixed shallow arches is much lower than the static value, resulting in a notable increase in the risk of dynamic instability [4]. In addition, transverse harmonic excitation can induce superharmonic resonance in functionally graded porous sinusoidal arches, and the characteristics of their resonant responses are significantly influenced by porosity and graphene platelet (GPL) content [5]. These dynamic loads, such as foundation vibrations caused by earthquakes, periodic excitations, and impacts, pose threats to arch structures, which highlights the necessity of conducting in-depth research on their dynamic stability.

Currently, most research on the in-plane dynamic instability of arch structures focuses on nonlinear dynamic buckling. From the perspective of load types, the dynamic buckling of shallow arches demonstrates a distinct load dependence. Specifically, under a point load applied at its crown, the arch exhibits bistable behavior. Arches with high modified slenderness ratios possess dual critical loads, whereas those with low ratios have only a single critical load [6]. Uneven constraint stiffness at rotational ends tends to induce multiple unstable branches [7]. Step radial point loads trigger asymmetric deformation. As the load deviates from the crown, the instability load first decreases, then increases, and beyond a specific position, the structure exhibits only stable vibrations [8]. For material properties, in functionally graded porous (FGP) arches, internal pores degrade load-bearing capacity, while graphene platelets (GPLs) enhance it. This pattern holds true even for constrained FGP arches, with the constraint effect strengthening as the central angle increases [9,10]. Functionally graded material (FGM) shallow arches feature multiple equilibrium states, and loads near the crown readily induce defect sensitivity [11]. The nonlinear characteristics of laminated arches are regulated by GPL weight fraction, pore distribution, and foundation stiffness [12]. For functionally graded multi-layer micro–nano arches under thermomechanical loads, nonlocal effects and couple stresses contrastingly influence buckling loads, while elevated temperature can directly induce an initial deflection [13]. Elastically supported FG-GPLRC arches can exhibit buckling mode transitions. Their instability patterns are jointly determined by GPL distribution, rotational constraints, and geometric parameters [14]. Micro–nanoscale FGP arches display size effects, and their frequency is influenced by nonlocal parameters, temperature fields, and elastic foundations [15]. In a coupled system of a shallow arch and an elastically constrained rigid body, the rigid body's moment of inertia and height critically govern the coupling efficiency [16].

As a critical factor inducing dynamic instability in arch structures, base-excitation has been studied primarily with a focus on the out-of-plane and in-plane parametric resonance instability of circular or sinusoidal arches. In contrast, research into in-plane nonlinear subharmonic resonance instability remains limited. The Bolotin method effectively identifies both T- and 2T-periodic instability regions for the out-of-plane dynamic parametric response of circular arches under vertical harmonic base-excitation. The arch's included angle and slenderness ratio are the principal parameters that significantly alter the critical excitation frequency [17]. Similar parametric studies on elastically restrained arches highlight the role of constraint stiffness and load localization in shifting instability regions and altering stability thresholds [18,19]. Under in-plane base-excitation, the dynamic instability of shallow arches is primarily controlled by their rise–span ratio, damping, and static load component. A key finding reveals that the 2T-period instability region possesses a markedly wider bandwidth than the T-period region [20]. Studies on composite and functionally graded porous graphene platelet-reinforced (FGP-GPL) arches further show that instability behavior is sensitive to ply orientation, pore distribution, and damping

ratio [21,22]. For fixed-end arches under central periodic loads, in-plane dynamic instability is strongly influenced by the rise–span ratio. A reduced rise–span ratio increases the critical frequency and its bandwidth, while a greater concentrated mass reduces both [23]. For FGP-GPL arches under combined static and dynamic loads, a symmetric non-uniform pore distribution coupled with a low GPL content significantly improves their resistance to dynamic instability [24]. Current research on base-excitation has predominantly addressed the linear parametric resonance instability of circular arches. In contrast, the in-plane nonlinear resonance instability, a phenomenon frequently encountered in engineering practice, has received limited attention.

Nonlinear resonance and the chaotic behavior of arch structures play a crucial role in revealing their dynamic instability mechanisms. Existing studies indicate that initial curvature, a key factor, can induce ½-superharmonic resonance in slightly curved beams, and nonlinear boundaries markedly alter their response characteristics [25]. In non-shallow arch systems, dynamic instability under harmonic loads can be analyzed using a two-degree-of-freedom reduced-order model, and the system exhibits rich periodic and aperiodic responses under 1:2 internal resonance conditions [26]. MEMS arches display 1:1 and 3:1 internal resonance behaviors under electrostatic excitation, where initial arch height determines the activation thresholds of different resonance modes [27]. In the context of chaotic dynamics, arches may develop chaotic bands under combined parametric and external forcing [28], and exhibit homoclinic orbits or quasi-periodic pulsations under specific excitation forms [29,30]. When vertical low-frequency excitation acts together with resonant harmonics, small-amplitude slow excitation effectively reduces the system's chaotic region [31]. Under base harmonic excitation, nonlinear curved beams demonstrate a rich variety of bifurcation behaviors. Once antisymmetric modes are activated, symmetry-breaking bifurcations emerge as a distinct dynamical feature [32]. Despite significant progress in understanding the internal resonance and chaotic bifurcation of arches, little attention has been given to their in-plane nonlinear subharmonic resonance, specifically the instability mechanisms under base-excitation.

Motivated by these identified gaps, this work is therefore dedicated to the in-plane nonlinear subharmonic resonance instability in fixed–fixed circular arches subjected to vertical harmonic base-excitation. Building on Hamilton's principle, a dynamic energy equation for the arch structure is established, incorporating the effects of von Kármán geometric nonlinearity. The Galerkin method is employed to discretize the system, reducing the partial differential equations to ordinary differential forms suitable for evaluating dimensionless fundamental frequencies and critical excitations. Subsequently, the method of multiple scales is used to construct the nonlinear subharmonic resonance curves and pinpoint the precise instability thresholds. Systematic analyses examine the effects of the circular arch's included angle, slenderness ratio, and damping ratio on its instability characteristics. The fourth-order Runge–Kutta method provides numerical solutions, which are further validated against finite element simulations. Furthermore, both the amplitude–frequency and force–response curves are also validated against Bolotin's method [33]. This approach confirms the accuracy of the theoretical model and clarifies the underlying mechanism of in-plane nonlinear dynamic instability triggered by subharmonic resonance. The findings directly inform the instability-resistant design of steel arches, with direct relevance to bridges and buildings. Furthermore, the presented model provides a foundation for analyzing arches of advanced materials, such as functionally graded and porous composites, broadening the scope of arch dynamics research.

2. Mathematical Formulations

2.1. In-Plane Kinematic Equation

Figure 1a depicts a fixed arch subjected to a vertical base-excitation $\ddot{\mathrm{V}}_t$, where the dashed lines denote the first-order in-plane antisymmetric mode. Key geometric parameters in this configuration are defined: S represents the arc length, 2Θ denotes the included angle, R stands for the initial radius of the arch, L is the span of the arch, $v(\varphi, t)$ and $w(\varphi, t)$ indicate the radial and tangential displacements, and refers to the angular coordinate. Figure 1b shows the cross-section of the arch.

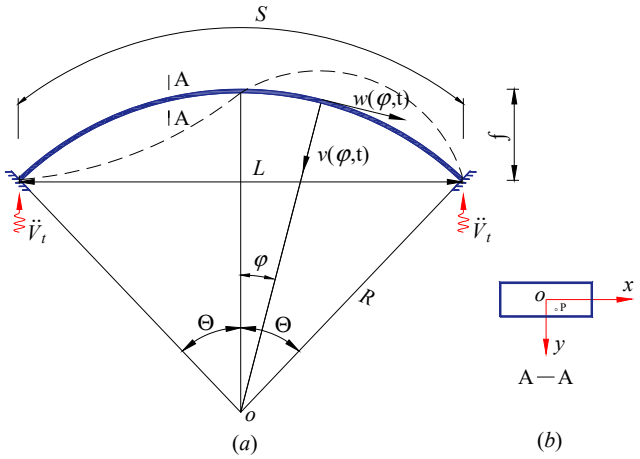

Figure 1. An arch under vertical base-excitation: (**a**) configuration, (**b**) cross-section.

As shown in Figure 1b, for any arbitrary point P in the arch's cross-section, the corresponding membrane strain ε_m and bending strain ε_b can be expressed as

$$\varepsilon_m = \widetilde{w}'(\varphi, t) - \widetilde{v}(\varphi, t) + \frac{1}{2}\widetilde{v}'^2(\varphi, t),\ \varepsilon_b = -y_p \frac{\widetilde{v}''(\varphi, t) + \widetilde{w}'(\varphi, t)}{R}, \tag{1}$$

where $(\,)' = \partial(\,)/\partial\varphi$, y_p is defined as the y-direction coordinate of point P, with the dimensionless radial displacement expressed as $\widetilde{v}(\varphi, t) = v(\varphi, t)/R$ and the tangential displacement as $\widetilde{w}(\varphi, t) = w(\varphi, t)/R$. For convenience, $\widetilde{v}(\varphi, t)$ and $\widetilde{w}(\varphi, t)$ are hereafter simplified to $\widetilde{v}$ and $\widetilde{w}$, respectively.

Under the assumption that shear deformation and rotary inertia are negligible, the kinetic energy T of the arch may be expressed as

$$T = \frac{1}{2}\rho A R^3 \int_{-\Theta}^{\Theta} \left(\dot{\widetilde{V}}^2 + \dot{\widetilde{W}}^2 \right) \mathrm{d}\varphi, \tag{2}$$

where A and ρ represent the cross-sectional area and mass density of the arch, respectively. The dimensionless radial and tangential displacements, $\widetilde{V} = V/R$ and $\widetilde{W} = W/R$, are given by [34]

$$\widetilde{V} = \widetilde{v} + \widetilde{\mathrm{V}}_t \cos(\varphi),\ \widetilde{W} = \widetilde{w} + \widetilde{\mathrm{V}}_t \sin(\varphi), \tag{3}$$

where $\widetilde{\mathrm{V}}_t = \mathrm{V}_t/R$ denotes the dimensionless vertical base displacement due to base-excitation.

The arch's strain energy U can be expressed as

$$U = \frac{1}{2}\int_{-\Theta}^{\Theta} \left[EAR\left(\widetilde{w}' - \widetilde{v} + \frac{1}{2}\widetilde{v}'^2 \right)^2 + \frac{EI_x}{R}\left(\widetilde{v}'' + \widetilde{w}' \right)^2 \right] \mathrm{d}\varphi, \tag{4}$$

where E is the elastic modulus, and I_x is the second moment of area.

The work done by the internal force W_N, associated with the dynamic longitudinal axial force $N(\varphi, \mathrm{t})$, is given by

$$W_N = \frac{1}{2}\int_{-\Theta}^{\Theta}\left[N(\varphi,t)\left(\widetilde{v}' + \widetilde{w}\right)^2\right] R d\varphi, \tag{5}$$

Moreover, the unconservative force work W_d from damping can be written as

$$W_d = \int_{-\Theta}^{\Theta}\left(F_{d\widetilde{v}}\widetilde{v} + F_{d\widetilde{w}}\widetilde{w}\right)R^2\,\mathrm{d}\varphi, \tag{6}$$

where the damping forces in the radial and tangential directions, $F_{d\widetilde{v}}$ and $F_{d\widetilde{w}}$, are given, respectively, by

$$F_{d\widetilde{v}} = -c_d R\dot{\widetilde{v}},\ F_{d\widetilde{w}} = -c_d R\dot{\widetilde{w}}, \tag{7}$$

where $c_d = 2\rho A\omega_n\xi$ is the damping coefficient [35], which relates directly to the arch's fundamental frequency ω_n and its damping ratio ξ.

The in-plane governing equations of the arch are derived from Hamilton's principle:

$$\int_{t_1}^{t_2}\delta\ell dt = \int_{t_1}^{t_2}\delta(T - U - W_d - W_N)dt = 0. \tag{8}$$

Subsequent substitution of Equations (2)–(7) into Equation (8), followed by the application of variational calculus, leads to the in-plane equilibrium differential equations:

$$\begin{gathered}\rho AR^3\ddot{\widetilde{v}} + F_{d\widetilde{v}}R^2 - EAR\left[\left(\widetilde{w}' - \widetilde{v} + \tfrac{1}{2}\widetilde{v}'^2\right)\left(1 + \widetilde{v}''\right) + \left(\widetilde{w}'' - \widetilde{v}' + \widetilde{v}'\widetilde{v}''\right)\widetilde{v}'\right] + \\ \tfrac{EI_x}{R}\left(\widetilde{v}'''' + \widetilde{w}''\right) + \rho AR^3\ddot{\widetilde{\mathrm{V}}}_t\cos(\varphi) - \left[N(\varphi,t)\left(\widetilde{v}' + \widetilde{w}\right)\right]' R = 0,\end{gathered} \tag{9}$$

and

$$\begin{gathered}\rho AR^3\ddot{\widetilde{w}} + F_{d\widetilde{w}}R^2 - EAR\left(\widetilde{w}'' - \widetilde{v}' + \widetilde{v}'\widetilde{v}''\right) - \tfrac{EI_x}{R}\left(\widetilde{v}'''' + \widetilde{w}''\right) + \rho AR^3\ddot{\widetilde{\mathrm{V}}}_t\sin(\varphi) \\ + N(\varphi,t)\left(\widetilde{v}' + \widetilde{w}\right)R = 0.\end{gathered} \tag{10}$$

where $\ddot{\widetilde{w}} = \partial^2\widetilde{w}/\partial t^2$, $\ddot{\widetilde{v}} = \partial^2\widetilde{v}/\partial t^2$. The base-excitation $\ddot{\widetilde{\mathrm{V}}}_t = \ddot{\mathrm{V}}_t/R$ is defined as

$$\ddot{\widetilde{\mathrm{V}}}_t = \frac{\mathrm{P}_t\cos(\Omega t)}{R} \tag{11}$$

Here, P_t represents the amplitude of the base-excitation. The arch's axial force $N(\varphi, t)$ is provided in [34]

$$N(\varphi,t) = \rho AR\ddot{\mathrm{V}}_t[(\lambda_1 - 1)\cos(\varphi) - \varphi\sin(\varphi)] \tag{12}$$

where the coefficient λ_1 is

$$\lambda_1 = -\frac{\begin{gathered}\left[\left(\Theta^2AR^2 + \Theta^2I_x\right) - 6AR^2\right]\cos(2\Theta) - \\ \tfrac{9}{2}\left(AR^2 + \tfrac{1}{3}I_x\right)\Theta\sin(2\Theta) + \left(-4AR^2 - 2I_x\right)\Theta^2 + 6AR^2\end{gathered}}{4AR^2\cos(2\Theta) + 2\Theta(AR^2 + I_x)\sin(2\Theta) + (4AR^2 + 4I_x)\Theta^2 - 4AR^2} \tag{13}$$

The axial displacements of shallow arches are quite small prior to buckling, so that their effects on the radial deformation may be ignored [36]. Accordingly, the inextensibility condition of the arch axis can be applied [21], i.e., no axial elongation or compression of the arch axis. Differentiation of Equation (9) with respect to the spatial coordinate, followed by subtracting Equation (10) and imposing the inextensibility condition, yields the final system governing the in-plane motion of a vertically excited circular arch.

$$\begin{aligned}\rho AR^3\left(\ddot{\widetilde{w}}''-\ddot{\widetilde{w}}\right)+\;& c_dR^3\left(\dot{\widetilde{w}}''-\dot{\widetilde{w}}\right)+\tfrac{EI_x}{R}\left(\widetilde{w}^{(6)}+2\widetilde{w}''''+\widetilde{w}''\right)-2\rho AR^3\ddot{\widetilde{V}}_t\sin(\varphi)\\ &-\left[N''(\varphi,t)\left(\widetilde{w}''+\widetilde{w}\right)+2N'(\varphi,t)\left(\widetilde{w}'''+\widetilde{w}'\right)\right.\\ &\left.+N(\varphi,t)\left(\widetilde{w}''''+2\widetilde{w}''+\widetilde{w}\right)\right]R\\ &-EAR\left(3\widetilde{w}''\widetilde{w}'''\widetilde{w}'''+\tfrac{3}{2}\widetilde{w}''\widetilde{w}''\widetilde{w}''''\right)=0\end{aligned}\tag{14}$$

2.2. Solution to the Kinematic Equation

A Galerkin projection recasts the tangential displacement into a modal superposition:

$$\widetilde{w}(\varphi,t)=\sum_{n=1}^{\infty}f_n(t)\phi_n(\varphi)\tag{15}$$

with $f_n(t)$ denoting the nth time-dependent amplitude and $\phi_n(\varphi)$ represents the tangential mode, as detailed in previous work [20].

By substituting Equation (15) into Equation (14) and applying the mode orthogonality principle, the in-plane equation of motion is transformed into a system of second-order ordinary differential equations

$$\ddot{\boldsymbol{f}}(\boldsymbol{t})+\mathfrak{R}_{1\boldsymbol{n}}\dot{\boldsymbol{f}}(\boldsymbol{t})+\mathfrak{R}_{2\boldsymbol{n}}\boldsymbol{f}(\boldsymbol{t})-\mathfrak{R}_{3\boldsymbol{n}}\ddot{V}_t\boldsymbol{f}(\boldsymbol{t})-\boldsymbol{f}_{\boldsymbol{N}}(\boldsymbol{t})=0,\tag{16}$$

where $\boldsymbol{f}(\boldsymbol{t})=[f_1(t),f_2(t),\ldots,f_n(t)]^{\boldsymbol{T}}$ contains the generalized coordinates governing in-plane motion, $\boldsymbol{f}_{\boldsymbol{N}}(\boldsymbol{t})$ collects the nonlinear contributions, and $\mathfrak{R}_{1\boldsymbol{n}},\mathfrak{R}_{2\boldsymbol{n}},\mathfrak{R}_{3\boldsymbol{n}}$ are $(N\times N)$ diagonal matrices whose components are explicitly given below:

$$\begin{aligned}\mathfrak{R}_{1n}&=2\omega_n\xi,\\ \mathfrak{R}_{2n}&=\tfrac{EI_x}{\rho AR^4}\,\frac{\int_{-\Theta}^{\Theta}\left[\phi_n^{(6)}(\varphi)+2\phi_n^{(4)}(\varphi)+\phi_n''(\varphi)\right]\phi_n(\varphi)\,\mathrm{d}\varphi}{\int_{-\Theta}^{\Theta}\left[\phi_n''(\varphi)-\phi_n(\varphi)\right]\phi_n(\varphi)\,\mathrm{d}\varphi},\\ &\int_{-\Theta}^{\Theta}N''(\varphi)\left[\phi_n''(\varphi)+\phi_n(\varphi)\right]\phi_n(\varphi)d\varphi+\\ &+2\int_{-\Theta}^{\Theta}N'(\varphi)\left[\phi_n'''(\varphi)+\phi_n'(\varphi)\right]\phi_n(\varphi)d\varphi+\\ \mathfrak{R}_{3n}&=\tfrac{1}{R}\,\frac{\int_{-\Theta}^{\Theta}N(\varphi)\left[\phi_n^{(4)}(\varphi)+2\phi_n''(\varphi)+\phi_n(\varphi)\right]\phi_n(\varphi)d\varphi}{\int_{-\Theta}^{\Theta}\left[\phi_n''(\varphi)-\phi_n(\varphi)\right]\phi_n(\varphi)\,\mathrm{d}\varphi}\end{aligned}\tag{17}$$

The natural frequencies ω_n^2 and the critical base-excitation $\ddot{V}_{n,\mathrm{cr}}$ for the arch are directly obtained by solving the eigenvalue problem:

$$\det\left[\mathbf{I}-\omega_n^2\mathfrak{R}_{2\boldsymbol{n}}=0\right]\tag{18}$$

$$\det\left[\mathfrak{R}_2-\ddot{V}_{\mathrm{n,cr}}\mathfrak{R}_3=0\right]\tag{19}$$

For a fixed–fixed arch under a vertical base-excitation, the first-order in-plane antisymmetric buckling mode closely resembles the corresponding free-vibration mode. This indicates that the first-order antisymmetric free-vibration mode can be used to approximate the first-order in-plane antisymmetric buckling mode. This similarity justifies approxi-

mating the first-order antisymmetric motion using a single-mode expansion [34], thereby avoiding the need for more complex multi-order approaches. The resulting simplification significantly accelerates the determination of the nonlinear resonance curve. Substituting n = 1 into Equations (16) and (17) turns the in-plane equation for the first-order antisymmetric motion into a second-order ordinary differential equation:

$$\ddot{f}(t) + \mathfrak{R}_{11}\dot{f}(t) + \mathfrak{R}_{21}f(t) - \mathfrak{R}_{31}\ddot{\mathrm{V}}_t f(t) - \mathfrak{R}_4 f^3(t) = 0 \tag{20}$$

where $f(t)$ is the time-dependent generalized coordinate of the first-order in-plane antisymmetric motion, $\mathfrak{R}_{11}, \mathfrak{R}_{21}, \mathfrak{R}_{31}$ are the matrix components with n = 1, and $\mathfrak{R}_4$ is given by

$$\mathfrak{R}_4 = \frac{E\int_{-\Theta}^{\Theta}\left[3\phi_1''(\varphi)\phi_1'''(\varphi)\phi_1'''(\varphi) + \frac{3}{2}\phi_1''(\varphi)\phi_1''(\varphi)\phi_1''''(\varphi)\right]\phi_1(\varphi)\,\mathrm{d}\varphi}{\rho R^2\int_{-\Theta}^{\Theta}\left[\phi_1''(\varphi) - \phi_1(\varphi)\right]\phi_1(\varphi)\,\mathrm{d}\varphi} \tag{21}$$

The in-plane nonlinear subharmonic resonance of an arch is investigated. Based on the method of multiple scales, Equation (20) can be further simplified by using the following transformation

$$\mathfrak{R}_{11} = \varepsilon\Gamma_1,\ \mathfrak{R}_{31} = \varepsilon\Gamma_3, \mathfrak{R}_4 = \varepsilon^2\Gamma_4 \tag{22}$$

where $\varepsilon = h/R$ is the small parameter. Substituting this relation into Equation (20) yields

$$\ddot{f}(t) + \varepsilon\Gamma_1\dot{f}(t) + \mathfrak{R}_{21}f(t) - \varepsilon\Gamma_3\ddot{\mathrm{V}}_t f(t) - \varepsilon^2\Gamma_4 f^3(t) = 0 \tag{23}$$

2.3. Instability of Nonlinear Subharmonic Resonance

To solve Equation (23), we apply the multiscale method and use a second-order approximation

$$f(t;\varepsilon) = \varepsilon^0 f_0(T_0, T_1, T_2) + \varepsilon^1 f_1(T_0, T_1, T_2) + \varepsilon^2 f_2(T_0, T_1, T_2) + o\left(\varepsilon^3\right) \tag{24}$$

here, $T_0 = \varepsilon^0 t$ is the fast time scale, while $T_1 = \varepsilon^1 t,\ T_2 = \varepsilon^2 t$ correspond to slow time scales. Following reference [37], the time derivative can be written as

$$\frac{\partial}{\partial t} = D_0 + \varepsilon D_1 + \varepsilon^2 D_2 + o\left(\varepsilon^3\right), \tag{25}$$

$$\frac{\partial^2}{\partial t^2} = D_0^2 + 2\varepsilon D_0 D_1 + \varepsilon^2\left(D_1^2 + 2D_0 D_2\right) + o\left(\varepsilon^3\right). \tag{26}$$

where $D_n = \frac{\partial}{\partial T_n}(n = 0, 1, 2)$.

After Equation (24) is substituted into Equation (23), the collection of coefficient terms corresponding to ε^0, ε^1, and ε^2 from both sides of the equation yields

$$\varepsilon^0 : D_0^2 f_0 + \omega_1^2 f_0 = 0, \tag{27}$$

$$\varepsilon^1 : D_0^2 f_1 + \omega_1^2 f_1 = -2D_0 D_1 f_0 - \Gamma_1 D_0 f_0 + \Gamma_3 f_0 \ddot{\mathrm{V}}_t, \tag{28}$$

$$\varepsilon^2 : D_0^2 f_2 + \omega_1^2 f_2 = -2D_0 D_1 f_1 - D_1^2 f_0 - 2D_0 D_2 f_0 - \Gamma_1 D_0 f_1 - \Gamma_1 D_1 f_0 + \Gamma_3 f_1 \ddot{\mathrm{V}}_t + \Gamma_4 f_0^3 \tag{29}$$

Solving Equation (27) yields

$$f_0(T_0, T_1, T_2) = A_1(T_1, T_2)\mathrm{e}^{i\omega_1 T_0} + \overline{A}_1(T_1, T_2)\mathrm{e}^{-i\omega_1 T_0} \tag{30}$$

where $A_1(T_1, T_2)$ denotes the undetermined complex amplitude and $\overline{A}_1(T_1, T_2)$ its complex conjugate. The parameter ω_1 corresponds to the in-plane first-order antisymmetric vibration frequency of a fixed–fixed circular arch.

Here, 1/2-subharmonic resonance is considered. Thus, the relationship between the base-excitation frequency and the first-order antisymmetric vibration frequency of the circular arch can be written as:

$$\Omega = 2\omega_1 + \varepsilon^2\sigma \tag{31}$$

Substituting Equation (31) into Equation (28) leads to

$$\begin{aligned} &D_0^2 f_1 + \omega_1^2 f_1 = -2i\Big(\tfrac{\partial}{\partial T_1}A_1(T_1, T_2)\Big)\omega_1 e^{i\omega_1 T_0} - i\Gamma_1 A_1(T_1, T_2)\omega_1 e^{i\omega_1 T_0} \\ &+\tfrac{1}{2}\Gamma_3 P_t A_1(T_1, T_2)e^{i(\Omega+\omega_1)T_0} + \tfrac{1}{2}\Gamma_3 P_t A_1(T_1, T_2)e^{i(\omega_1-\Omega)T_0} + cc \end{aligned} \tag{32}$$

where cc represents the complex conjugate of the known terms in Equation (32).

The solvability condition is derived by eliminating the secular terms in Equation (32):

$$2i\omega_1\left(\frac{\partial}{\partial T_1}A_1(T_1, T_2)\right) = -i\Gamma_1 A_1(T_1, T_2)\omega_1 + \frac{1}{2}\Gamma_3 P_t\overline{A}_1(T_1, T_2)e^{i(\Omega-\omega_1)T_0} \tag{33}$$

This leads to the non-homogeneous solution to Equation (28)

$$f_1 = -\frac{1}{2}\frac{\Gamma_3 P_t A_1(T_1, T_2)e^{i(\Omega+\omega_1)T_0}}{\Omega(\Omega+2\omega_1)} - \frac{1}{2}\frac{\Gamma_3 P_t\overline{A}_1(T_1, T_2)e^{-i(\Omega+\omega_1)T_0}}{\Omega(\Omega+2\omega_1)} \tag{34}$$

For the nonlinear subharmonic resonance described by Equation (31), the substitution of Equations (30) and (34) into Equation (29) and subsequent elimination of secular terms yield the solvability condition for the second-order expansion:

$$\begin{aligned} &2i\omega_1\left(\tfrac{\partial}{\partial T_2}A_1(T_1, \quad T_2)\right) \\ &\qquad = \tfrac{1}{4}\Gamma_1^2 A_1(T_1, T_2) - \tfrac{1}{4}\tfrac{\Gamma_3 P_t\overline{A}_1(T_1,T_2)e^{i\sigma\varepsilon T_1}}{\omega_1} - \tfrac{1}{4}\tfrac{\Gamma_3^2 P_t^2 A_1(T_1,T_2)}{\Omega(\Omega+2\omega_1)} \\ &\qquad -\tfrac{\Gamma_3^2 P_t^2 A_1(T_1,T_2)}{16\omega_1^2} + 3\Gamma_4 A_1(T_1, T_2)^2\overline{A}_1(T_1, T_2) \end{aligned} \tag{35}$$

After multiplying both sides of Equation (25) by $2i\omega_1$ and introducing $A_1(T_1, T_2)$, the following expression is

$$2i\omega_1\frac{\partial}{\partial t}A_1(T_1, T_2) = 2i\omega_1\varepsilon\left(\frac{\partial}{\partial T_1}A_1(T_1, T_2)\right) + 2i\omega_1\varepsilon^2\left(\frac{\partial}{\partial T_2}A_1(T_1, T_2)\right) + o\left(\varepsilon^3\right) \tag{36}$$

Substituting Equations (33) and (35) into Equation (36) yields

$$\begin{aligned} &\tfrac{\partial}{\partial t}A_1(T_1, T_2) - \varepsilon\Big[-i\Gamma_1 A_1(T_1, T_2)\omega_1 + \tfrac{1}{2}\Gamma_3 P_t\overline{A}_1(T_1, T_2)e^{i\sigma\varepsilon^2 t}\Big] + \\ &\varepsilon^2\left[\tfrac{1}{4}\Gamma_1^2 A_1(T_1, T_2) - \tfrac{1}{4}\tfrac{\Gamma_3 P_t\overline{A}_1(T_1,T_2)e^{i\sigma\varepsilon^2 t}}{\omega_1} - \tfrac{1}{4}\tfrac{\Gamma_3^2 P_t^2 A_1(T_1,T_2)}{\Omega(\Omega+2\omega_1)} - \tfrac{\Gamma_3^2 P_t^2 A_1(T_1,T_2)}{16\omega_1^2} + 3\Gamma_4 A_1(T_1, T_2)^2\overline{A}_1(T_1, T_2)\right] = 0 \end{aligned} \tag{37}$$

Solving Equation (37) allows the amplitude $A_1(T_1, T_2)$ to be expressed in the polar form given by

$$A_1(T_1, T_2) = \frac{1}{2}ae^{i\beta} \tag{38}$$

here, the real functions a and β denote the steady-state amplitude and phase of motion, respectively.

Substituting Equation (38) into Equation (37), separating the real and imaginary parts, it can be derived as below:

$$\dot{a} = -\frac{1}{2}a\Gamma_1\varepsilon - \left(\frac{\varepsilon^3\Gamma_3 P_t\sigma a}{8\omega_1^2} - \frac{\varepsilon\Gamma_3 P_t a}{4\omega_1}\right)sin\left(\sigma\varepsilon^2 t - 2\beta\right) \tag{39}$$

$$\begin{aligned} a\dot{\beta} = &-\frac{\varepsilon^2\Gamma_1^2 a}{8\omega_1} + \left(\frac{\varepsilon^3\Gamma_3 P_t\sigma a}{8\omega_1^2} - \frac{\varepsilon\Gamma_3 P_t a}{4\omega_1}\right)cos\left(\sigma\varepsilon^2 t - 2\beta\right) + \frac{\varepsilon^3\Gamma_3^2 P_t^2 a}{32\omega_1^3} \\ &+\frac{1}{8\omega_1}\frac{a\Gamma_3^2 P_t^2}{\Omega(\Omega+2\omega_1)} - \frac{3\varepsilon^2\Gamma_4 a^3}{8\omega_1} \end{aligned} \tag{40}$$

where the new phase angle is defined as $\eta = \sigma\varepsilon^2 t - 2\beta$. Then, the above equations can be rewritten as

$$\dot{a} = -\frac{1}{2}a\Gamma_1\varepsilon - \left(\frac{\varepsilon^3\Gamma_3 P_t\sigma a}{8\omega_1^2} - \frac{\varepsilon\Gamma_3 P_t a}{4\omega_1}\right)sin(\eta) \tag{41}$$

$$\begin{aligned} a\dot{\eta} = &a\sigma\varepsilon^2 + \frac{\varepsilon^2\Gamma_1^2 a}{4\omega_1} - \left(\frac{\varepsilon^3\Gamma_3 P_t\sigma a}{4\omega_1^2} - \frac{\varepsilon\Gamma_3 P_t a}{2\omega_1}\right)cos(\eta) - \frac{\varepsilon^3\Gamma_3^2 P_t^2 a}{16\omega_1^3} \\ &-\frac{1}{4\omega_1}\frac{a\Gamma_3^2 P_t^2}{\Omega(\Omega+2\omega_1)} + \frac{3\varepsilon^2\Gamma_4 a^3}{4\omega_1} \end{aligned} \tag{42}$$

Under steady-state conditions, the time derivatives $\dot{a}$ and $a\dot{\eta}$ in Equations (41) and (42) vanish. To seek a non-trivial solution ($a \neq 0$), the subsequent analysis requires that the amplitude and phase of the response satisfy

$$\frac{1}{2}\Gamma_1\varepsilon + \left(\frac{\varepsilon^3\Gamma_3 P_t\sigma}{8\omega_1^2} - \frac{\varepsilon\Gamma_3 P_t}{4\omega_1}\right)sin(\eta) = 0 \tag{43}$$

$$\begin{aligned} \sigma\varepsilon^2 + \frac{\varepsilon^2\Gamma_1^2}{4\omega_1} - \left(\frac{\varepsilon^3\Gamma_3 P_t\sigma}{4\omega_1^2} - \frac{\varepsilon\Gamma_3 P_t}{2\omega_1}\right)cos(\eta) - \frac{\varepsilon^3\Gamma_3^2 P_t^2}{16\omega_1^3} - \frac{1}{4\omega_1}\frac{\Gamma_3^2 P_t^2}{\Omega(\Omega+2\omega_1)} \\ +\frac{3\varepsilon^2\Gamma_4 a^2}{4\omega_1} = 0 \end{aligned} \tag{44}$$

From Equation (44), the backbone curve expression is derived as

$$a = -\frac{2\sqrt{-3\sigma\Gamma_4\omega_1}}{3\Gamma_4} \tag{45}$$

Eliminating η from Equations (43) and (44), followed by squaring and adding them, yields the frequency response equation

$$\left(\frac{\sigma\varepsilon^2 + \frac{\varepsilon^2\Gamma_1^2}{4\omega_1} - \frac{\varepsilon^3\Gamma_3^2 P_t^2}{16\omega_1^3} - \frac{1}{4\omega_1}\frac{\Gamma_3^2 P_t^2 A_1(T_1,T_2)}{\Omega(\Omega+2\omega_1)} + \frac{3\varepsilon^2\Gamma_4 a^2}{4\omega_1}}{\frac{\varepsilon^3\Gamma_3 P_t\sigma}{4\omega_1^2} - \frac{\varepsilon\Gamma_3 P_t}{2\omega_1}}\right)^2 + \frac{16\Gamma_1^2\omega_1^4}{\Gamma_3^2 P_t^2(\sigma\varepsilon^2 - 2\omega_1)^2} = 1 \tag{46}$$

To determine the stability of the nontrivial solution, one lets

$$a = a_0 + a_1,\ \eta = \eta_0 + \eta_1 \tag{47}$$

here, a_0, η_0 correspond to the solutions of Equations (43) and (44), while a_1,η_1 are perturbations which are assumed to be small compared to a_0 and η_0. Substituting (47) into Equations (43) and (44) and keeping only the linear terms in a_1 and η_1, we obtain

$$\boldsymbol{J} = \begin{bmatrix} 0 & \frac{\sigma\varepsilon^2 + \frac{\varepsilon^2\Gamma_1^2}{4\omega_1} - \frac{\varepsilon^3\Gamma_3^2 P_t^2}{16\omega_1^3} - \frac{1}{4\omega_1}\frac{\Gamma_3^2 P_t^2}{\Omega(\Omega+2\omega_1)} + \frac{3\varepsilon^2\Gamma_4 a^2}{4\omega_1}}{\frac{\varepsilon^3\Gamma_3 P_t\sigma}{4\omega_1^2} - \frac{\varepsilon\Gamma_3 P_t}{2\omega_1}} \\ \frac{3\varepsilon^2\Gamma_4}{2\omega_1} & \frac{\frac{1}{2}\Gamma_1\varepsilon}{\left(\frac{\varepsilon^3\Gamma_3 P_t\sigma}{8\omega_1^2} - \frac{\varepsilon\Gamma_3 P_t}{4\omega_1}\right)} \end{bmatrix} \tag{48}$$

where $\boldsymbol{J}$ is the Jacobian matrix.

The eigenvalues of $\boldsymbol{J}$ in Equation (48) are given by the following equation

$$P(\lambda) = b_0\lambda^2 + b_1\lambda + b_2 \tag{49}$$

Employing the Routh–Hurwitz criterion,

$$D_1 = b_1 > 0, D_2 = b_1 b_2 > 0 \tag{50}$$

the stability condition of nontrivial solution can be obtained. A solution is stable when all eigenvalues exhibit negative real parts. Conversely, it is rendered unstable if at least one eigenvalue possesses a positive real part.

3. Validation

3.1. Fundamental Frequency

A finite element model of the arch under vertical base-excitation was established in ANSYS 17 to verify the present method for determining the fundamental frequency and critical base-excitation associated with the in-plane antisymmetric mode. The parameters are selected as follows: density $\rho = 2700$ kg/m^3, Young's modulus $E = 6.538 \times 10^{10}$ pa, Poisson's ratio $\mu = 0.33$, and the rectangular section dimensions $b \times h = 0.02$ m $\times$ 0.002 m. The BEAM4 element was selected as the discretization unit to simulate the arch structure. The arch axis was uniformly divided into 100 elements to ensure mesh density and calculation accuracy, and a preliminary mesh convergence check for the fundamental frequency confirmed the rationality of this mesh scheme. Regarding boundary conditions, fixed-end constraints were imposed at both endpoints of the arch, restricting all translational displacements and rotational displacements.

The natural frequency and critical base-excitation are solved using Equations (18) and (19). To simplify subsequent analysis, the following non-dimensional parameters are defined:

$$\omega_n^* = R^2\omega_n\sqrt{\frac{\rho A}{EI_x}} \tag{51}$$

$$\ddot{V}_{cr,n}^* = \ddot{V}_{cr,n}L^3/EI_x \tag{52}$$

Pi [38] proposed that an included angle of $2\Theta = 90^\circ$ be adopted as the criterion distinguishing shallow from non-shallow arches. Accordingly, circular arches with included angles of $2\Theta = 60^\circ$, 90° and 120° are investigated in this study. For a given included angle, both the rise-to-span ratio (f/L) and radius-to-span ratio (R/L) remain constant irrespective of the slenderness ratio. Conversely, at a fixed slenderness ratio, f/L increases while R/L decreases with increasing included angle. It should be noted that f/L and R/L are uniquely determined by the included angle and are independent of the slenderness ratio. Hereafter, variations in the included angle implicitly denote corresponding changes in f/L and R/L, which will not be reiterated for brevity.

Table 1 presents a comparison of the dimensionless fundamental frequency ω_1^* for an arch at a varying included angle 2Θ and slenderness ratio S/r_x. Results reveal that, with the 2Θ held constant, the frequency ω_1^* and the error remain unchanged as the slenderness ratio increases. In contrast, when the slenderness ratio S/r_x is kept constant, the frequency ω_1^* decreases and error increases gradually as the 2Θ grows. Additionally, the theoretical solutions obtained in this study exhibit strong consistency with the finite element method (FEM) results.

Table 1. Comparison of the dimensionless fundamental frequency ω_1^* of the arch with different included angles 2Θ and slenderness ratios S/r_x ($S = 2\Theta R, r_x = \sqrt{I_x/A}$).

S/r_x / 2Θ, f/L,R/L	S/r_x=800			S/r_x=1200			S/r_x=1600		
	Present	**FEM**	**Error**	**Present**	**FEM**	**Error**	**Present**	**FEM**	**Error**
$2\Theta = 60^\circ$ ($f/L = 0.13, R/L = 1$)	53.740	53.740	0%	53.740	53.740	0%	53.740	53.740	0%
$2\Theta = 90^\circ$ ($f/L = 0.21, R/L = 0.71$)	22.625	22.628	0.01%	22.625	22.628	0.01%	22.625	22.628	0.01%
$2\Theta = 120^\circ$ ($f/L = 0.29, R/L = 0.58$)	11.848	11.851	0.03%	11.848	11.851	0.03%	11.848	11.851	0.03%

Notes: Error = $|(\text{Present} - \text{FEM})/\text{FEM} \times 100\%|$.

Table 2 compares the dimensionless critical base-excitations of the arch under different included angles 2Θ and slenderness ratios S/r_x. The results reveal that when the included angle is fixed, the dimensionless critical base-excitation decreases gradually as the slenderness ratio increases. Conversely, with the slenderness ratio kept constant, the dimensionless critical base-excitation increases progressively as the included angle grows. While the values of the dimensionless critical base-excitation calculated via the method proposed in this study exhibit slight deviations from the FEM results, all errors are within 2.5%, and the outcomes from both methods demonstrate good consistency.

Table 2. Comparison of the dimensionless critical base-excitation $\ddot{V}_{n,cr}$ of the arch with different included angles 2Θ and slenderness ratios S/r_x ($S = 2\Theta R, r_x = \sqrt{I_x/A}$).

S/r_x / 2Θ, f/L,R/L	S/r_x=800			S/r_x=1200			S/r_x=1600		
	Present	**FEM**	**Error**	**Present**	**FEM**	**Error**	**Present**	**FEM**	**Error**
$2\Theta = 60^\circ$ ($f/L = 0.13, R/L = 1$)	717.29	700.96	2.33%	716.89	700.56	2.33%	716.75	700.45	2.33%
$2\Theta = 90^\circ$ ($f/L = 0.21, R/L = 0.71$)	925.35	904.56	2.30%	925.14	904.37	2.30%	925.06	904.26	2.30%
$2\Theta = 120^\circ$ ($f/L = 0.29, R/L = 0.58$)	976.96	956.85	2.10%	976.84	956.73	2.10%	976.80	956.71	2.10%

Notes: Error = $|(\text{Present} - \text{FEM})/\text{FEM} \times 100\%|$.

3.2. Frequency– and Force–Response Curves

A fixed–fixed circular arch with an included angle of $2\Theta = 60^\circ$ and a slenderness ratio of $S/r_x = 800$ is selected for validation, with parameters set as $\xi = 0.1$ and $P_t = 0.5\ddot{V}_{cr,1}$. Figure 2 illustrates the dimensionless amplitude–frequency curve for the in-plane nonlinear vibration of the arch under vertical base-excitation, where the vertical axis represents the dimensionless vibration amplitude and the horizontal axis corresponds to the dimensionless excitation frequency. Solid lines denote stable solutions, and dashed lines denote unstable solutions.

As shown in Figure 2, the dimensionless excitation frequency is divided into three distinct regions:

Region 1: $\Omega/\omega_1 < \omega_L^*$;

Region 2: $\omega_L^* < \Omega/\omega_1 < \omega_H^*$;

Region 3: $\Omega/\omega_1 > \omega_H^*$.

In Region 1, the vibration amplitude remains nearly zero, indicating that the energy from vertical excitation is insufficient to induce significant nonlinear vibration. Region 2 represents stable vibration, where the solid line denotes the stable response. The black backbone curve from the Region 2 reflects the hardening nonlinearity characteristic of the 1/2-subharmonic resonance in the arch. Region 3 is identified as the unstable zone, where

the dynamic system is prone to complex behaviors. At a dimensionless amplitude of $a/h = 0$, a specific dimensionless excitation frequency, denoted as $\omega_b^* = 2$, is observed along the backbone curve.

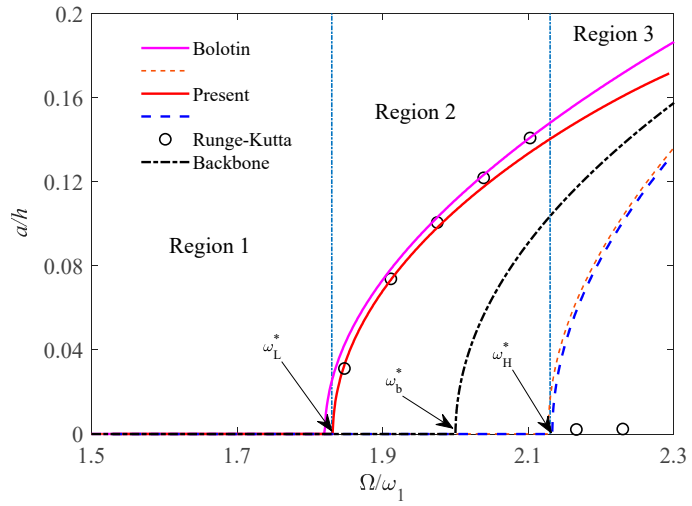

Figure 2. Comparison of the dimensionless amplitude–frequency curve calculated by present method with that by Runge–Kutta method and Bolotin's method [33].

The dimensionless amplitude–frequency curve was compared with both the Runge–Kutta method and Bolotin's method [33]. The comparison reveals that the present method yields results in very close agreement with the Runge–Kutta method, while exhibiting a slight deviation from Bolotin's method. This discrepancy is primarily attributed to the fact that Bolotin's method is based on a first-order approximation of $f(t)$, whereas the method of multiple scales employed here utilizes a second-order approximation.

In Figure 3, the base-excitation frequency is set to $\Omega = 1.9\omega_1$, while all other parameters remain identical to those in Figure 2. The remarkable agreement between the dimensionless force–response curve obtained by the present method and the results from the Runge–Kutta approach and Bolotin's method clearly validates the accuracy of the present methodology.

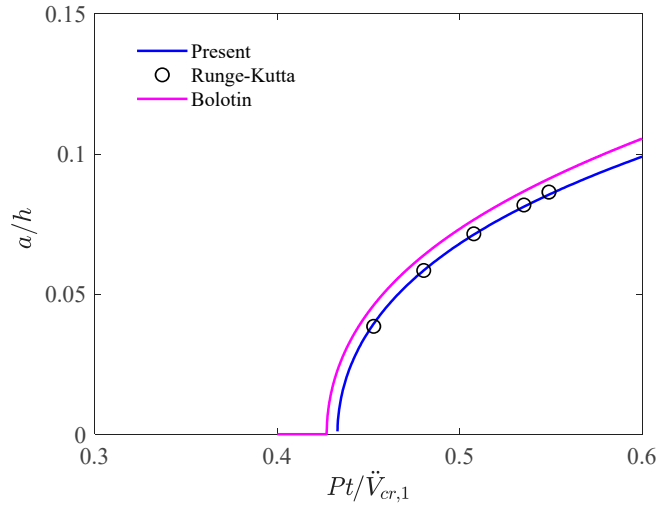

Figure 3. Comparison of the dimensionless force–response curve calculated by present method with that by Runge–Kutta method and Bolotin's method [33].

4. Discussion

This section provides a detailed discussion of the results. However, before presenting the results, the dynamic model of the arch used in this study is first described. Employing Bernoulli arch theory, this work neglects shear deformation and rotational inertia, assumes ideal fixed ends at the arch's two extremities, and adopts linear damping. It is noted that this damping model's applicability is limited when material or contact nonlinearity becomes dominant. The study investigates the in-plane first-order antisymmetric nonlinear subharmonic resonance instability of circular arches subjected to vertical base-excitation. It should be noted that the single-mode truncation of this model cannot capture higher-mode coupling behaviors such as internal resonance, and this limitation will be the focus of subsequent research efforts.

4.1. Effect of Included Angle

Figure 4 presents the dimensionless amplitude–frequency curves for in-plane nonlinear 1/2-subharmonic resonance of circular arches with varying included angles under vertical base-excitation. The parameters are specified as follows: the slenderness ratio $S/r_x = 800$, $\xi = 0.08$, and $P_t = 0.4\ddot{V}_{cr,1}$, where $\ddot{V}_{cr,1}$ denotes the critical base-excitation at $2\Theta = 120°$.

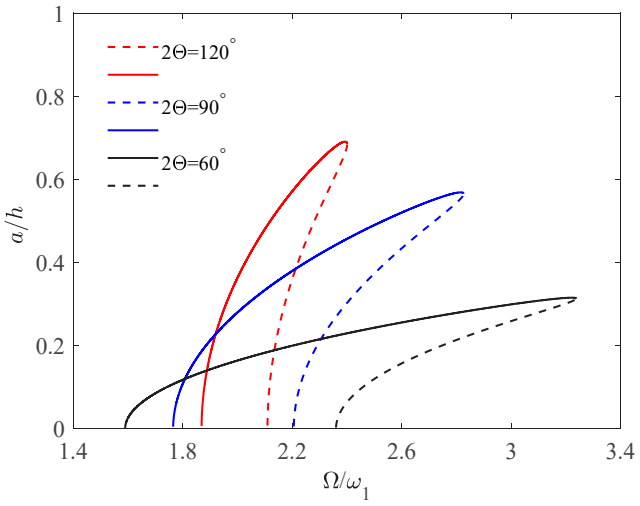

Figure 4. Dimensionless amplitude–frequency curves under different included angles.

All response curves exhibit hardening-type nonlinear behavior, characterized by a nonlinear increase in dimensionless amplitude with rising excitation frequency and the formation of distinct resonant peaks. Notably, the arch with $2\Theta = 120°$ demonstrates the most pronounced vibration peak and the steepest curve growth, whereas the $2\Theta = 60°$ configuration shows the lowest amplitude peak and the most gradual growth trend. While larger included angles lead to higher critical base-excitation, this effect is counteracted by a concurrent reduction in nonlinear and damping coefficients. The net result is a diminished nonlinearity and a consequent amplification of the dimensionless amplitude–frequency response. Furthermore, the arch with $2\Theta = 60°$ exhibits the broadest stable vibration region (Region 2), as evidenced by its maximum dimensionless frequency range ($\omega_H^* - \omega_L^*$).

To examine the evolution of the dimensionless force–response curve under two distinct excitation frequencies, specifically selected to represent cases above and below $\omega_b^* = 2$, the frequencies chosen are $\Omega/\omega_1 = 1.95$ (where $\omega_L^* < \Omega/\omega_1 < \omega_b^* = 2$) and $\Omega/\omega_1 = 2.05$ (where $\omega_H^* > \Omega/\omega_1 = 2.05 > \omega_b^* = 2$). The corresponding force–response curves are derived, with $\ddot{V}_{cr,1}$ defined as the critical base-excitation for arches with included angles $2\Theta = 60°$, $90°$, and $120°$.

When the excitation frequency remains below the threshold for 1/2-subharmonic resonance, nonlinear effects are suppressed, and the system response is dominated by linear vibration. Consequently, the force–response curve exhibits a single-valued, monotonically increasing behavior, as shown in Figure 5.

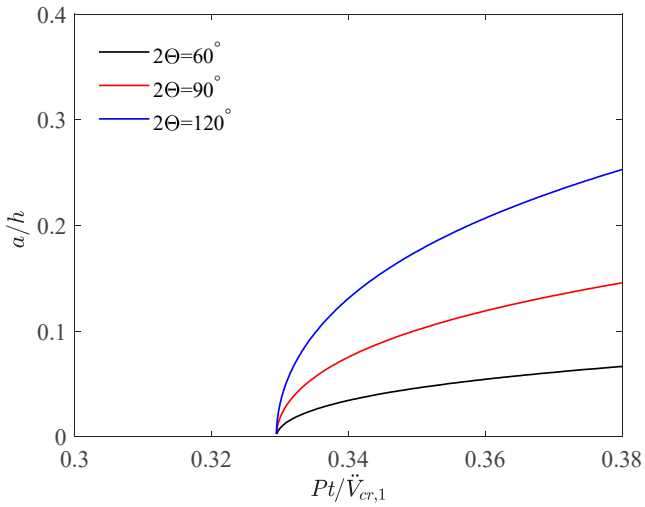

Figure 5. Dimensionless force–response curves under different included angles when $\omega_L^* < \Omega/\omega_1 = 1.95 < \omega_b^*$.

Figure 6 displays the dimensionless force–response curves corresponding to the excitation frequency $\Omega/\omega_1 = 2.05$, which satisfies $\omega_H^* > \Omega/\omega_1 > \omega_b^* = 2$. The response curves manifest characteristic saddle-node bifurcation behavior, marked by multistability and multi-valued solutions, indicating that the dynamic system undergoes multistable oscillations under this condition. Bifurcation behavior is observed across all included angles, with larger angles leading to a more pronounced bifurcation magnitude and wider multi-solution intervals. The stable solution, represented by the solid line, shows an increasing dimensionless response with greater force amplitude, while the unstable solution, depicted by the dashed line, displays a decreasing trend. Furthermore, although the dimensionless excitation threshold $P_t/\ddot{V}_{cr,1}$ for the onset of bifurcation remains nearly identical across different included angles, the corresponding dimensionless response threshold increases with larger angles.

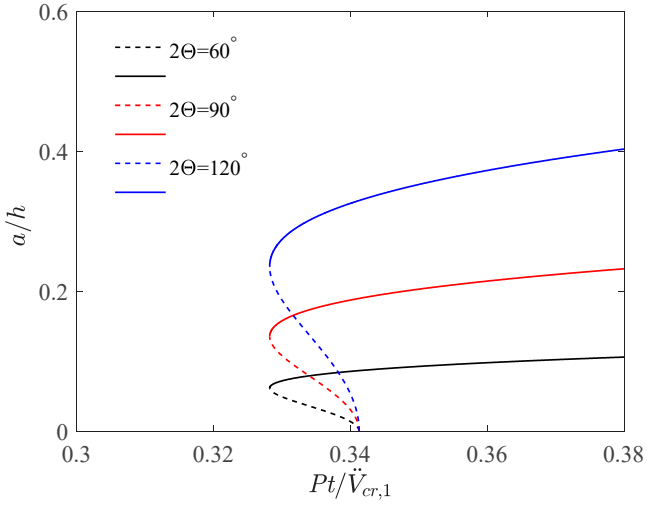

Figure 6. Dimensionless force–response curves under different included angles when $\omega_H^* > \Omega/\omega_1 = 2.05 > \omega_b^*$.

4.2. Effect of Slenderness Ratio

The dynamic response is analyzed for an arch with an included angle of $2\Theta = 90^\circ$ under varying slenderness ratios ($S/r_x = 800, 900, 1000$). The analysis employs a damping ratio of $\xi = 0.08$ and an excitation load equal to 0.4 times the critical base-excitation. Here, the critical base-excitation amplitude refers to that of the arch with $S/r_x = 800$ and $2\Theta = 90^\circ$. With an increasing slenderness ratio, both the damping coefficient and the critical base-excitation of the arch decrease. As a result, the arch becomes more flexible, and the nonlinear effects in the dynamic system are enhanced. This leads to a shift in the peak frequency of the amplitude–frequency curve toward higher values, as illustrated in Figure 7.

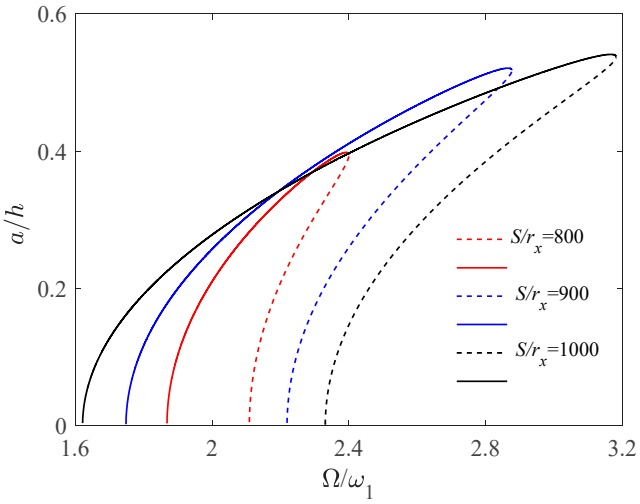

Figure 7. Dimensionless amplitude–frequency curves under different slenderness ratios.

Figures 8 and 9 present the dimensionless force–response curves obtained at excitation frequencies $\Omega/\omega_1 = 1.95$ (where $\omega_L^* < \Omega/\omega_1 < \omega_b^* = 2$) and $\Omega/\omega_1 = 2.05$ (where $\omega_H^* > \Omega/\omega_1 > \omega_b^* = 2$), respectively. Here, $\ddot{V}_{cr,1}$ denotes the critical base-excitation for arches with slenderness ratios $S/r_x = 800$, 900, and 1000.

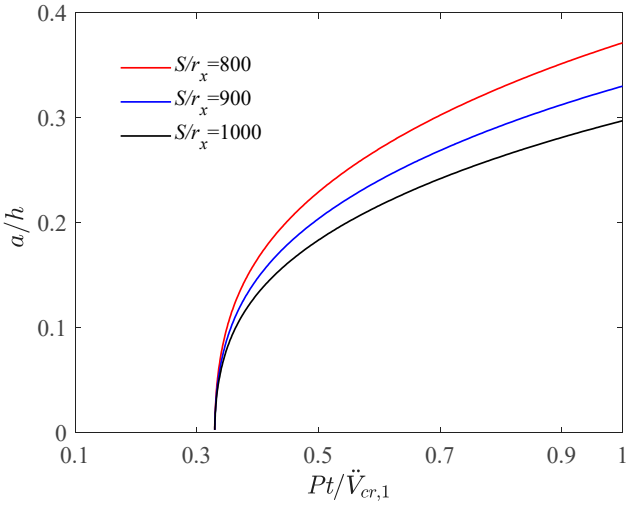

Figure 8. Dimensionless force–response curves under different slenderness ratios when $\omega_L^* < \Omega/\omega_1 = 1.95 < \omega_b^*$.

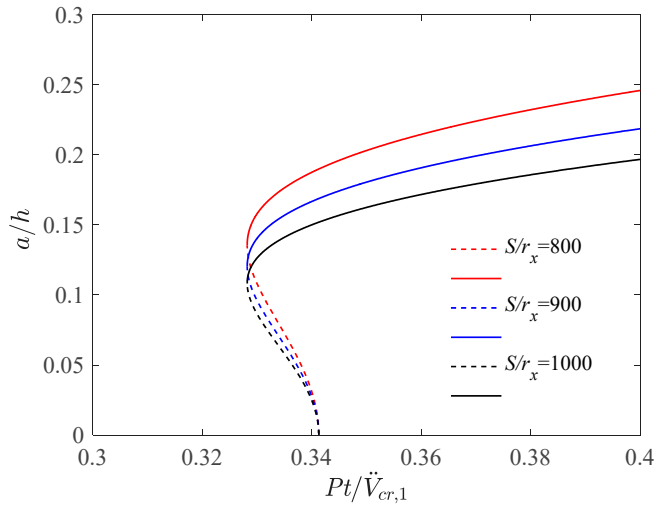

Figure 9. Dimensionless force–response curves under different slenderness ratios when $\omega_H^* > \Omega/\omega_1 = 2.05 > \omega_b^*$.

As shown in Figure 8, under the selected frequency condition $\omega_L^* < \Omega/\omega_1 = 1.95 < \omega_b^* = 2$, the arch exhibits in-plane antisymmetric stable vibration. The dimensionless response *a/h* increases with the dimensionless base-excitation amplitude for all three slenderness ratios. Moreover, at a given excitation amplitude, the response decreases as the slenderness ratio increases.

In contrast, the response curves in Figure 9, corresponding to $\omega_H^* > \Omega/\omega_1 > \omega_b^* = 2$, display saddle-node bifurcation characteristics across all slenderness ratios. With increasing dimensionless force, the stable solution (solid line) shows an increasing trend, while the unstable solution (dashed line) decreases. Although the normalized excitation threshold $\mathrm{P}_t/\ddot{\mathrm{V}}_{cr,1}$ for the onset of bifurcation remains nearly identical with increasing slenderness ratio, the corresponding dimensionless response threshold decreases.

4.3. Effect of Damping Ratio

An arch with an included angle of 60° and a slenderness ratio of 800 is selected for analysis, under a base-excitation amplitude of $\mathrm{P}_t = 0.4\ddot{\mathrm{V}}_{cr,1}$. As illustrated in Figure 10, a smaller damping ratio leads to a higher peak dimensionless response occurring over a wider excitation frequency range ($\omega_H^* - \omega_L^*$), whereas a larger damping ratio significantly reduces the response amplitude. The nonlinear jump phenomenon, indicated by the separation between the solid and dashed curves in the amplitude–frequency curve, becomes more pronounced under lower damping conditions. This behavior clearly reflects the hardening characteristics of the nonlinear vibration in weakly damped systems.

Figure 11 shows the dimensionless force–response curve corresponding to the excitation frequency condition $\omega_L^* < \Omega/\omega_1 = 1.95 < \omega_b^* = 2$. As the damping ratio increases, the normalized excitation threshold required to initiate the response shifts to higher values, while the corresponding dimensionless response amplitude diminishes.

In contrast, Figure 12 presents the response curve under the frequency condition $\omega_H^* > \Omega/\omega_1 = 2.05 > \omega_b^*$. With an increasing damping ratio, the normalized excitation threshold for bifurcation onset rises notably, and the dimensionless response level decreases accordingly.

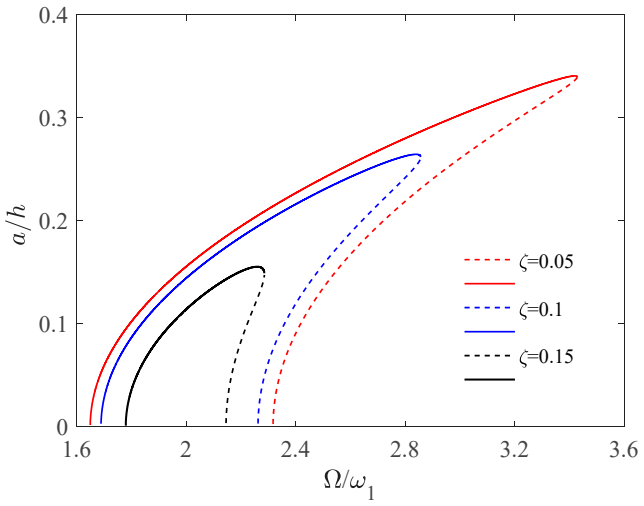

Figure 10. Dimensionless amplitude–frequency curves under different damping ratios.

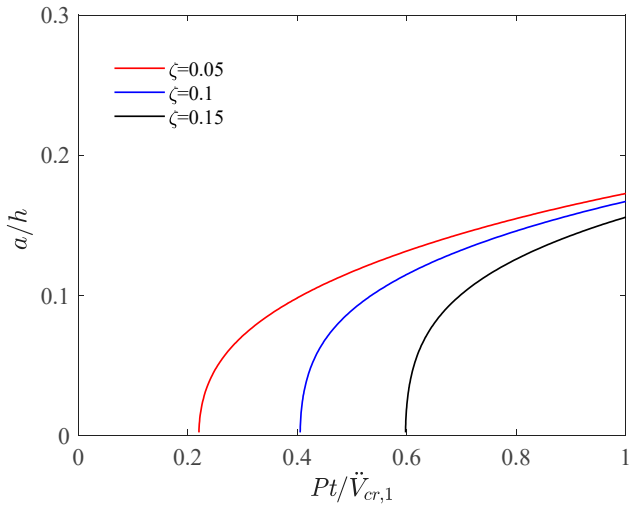

Figure 11. Dimensionless force–response curves under different damping ratios when $\omega_L^* < \Omega/\omega_1 = 1.95 < \omega_b^*$.

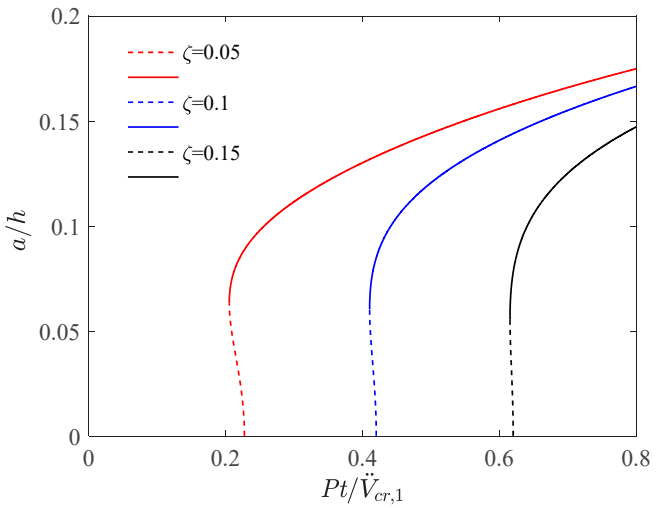

Figure 12. Dimensionless force–response curves under different damping ratios when $\omega_H^* > \Omega/\omega_1 = 2.05 > \omega_b^*$.

5. Conclusions

This study focuses on investigating the nonlinear 1/2-subharmonic resonance of an arch under a vertical base-excitation. An analytical model was developed to capture this dynamic behavior, and the model underwent rigorous validation via finite element simulations. Notably, a critical frequency $\omega_b^* = 2$ was identified that delineates distinct dynamic response regions. Two distinct behaviors define these regions. Below this critical frequency, the arch's vibration remains stable and monotonic. Above this critical frequency, multiple stable states can coexist, accompanied by sudden jumps in the dynamic response. The dynamic response of the arch is primarily influenced by three key parameters. Larger included angles lead to increased vibration amplitudes but reduce the range of stable operation. Higher slenderness ratios improve structural flexibility and intensify nonlinear dynamic effects. In contrast, greater damping effectively diminishes vibration amplitude and helps suppress the emergence of unstable dynamic behavior. In summary, the methodology developed herein allows for a precise assessment of dynamic stability in arch structures, guiding the design of systems in civil engineering and MEMSs against resonant failure.

Author Contributions: Conceptualization, Z.Z. and F.S.; Methodology, Z.Z.; Software, Z.Z. and W.X.; Funding acquisition, Z.Z. and X.X.; Validation, Z.Z., Z.Y. and X.X.; Writing—original draft, Z.Z.; Supervision, F.S. and W.X.; Visualization, Z.Y.; Resources, X.X.; Formal Analysis, W.X. All authors have read and agreed to the published version of the manuscript.

Funding: This research was funded by the Newly Introduced Human Resources-Related Program (Grant NO. GTXY2201], the Engineering Technology Research and Development Center for Colleges and Universities of Guangdong Province (Grant No.2024GCZX018), the University Research Program of Guangzhou (Grant No.2024312485), and the Rail Transit Line-Bridge-Tunnel Intelligent Monitoring, Detection and Safety Prevention & Control Technology Innovation Team (Grant No. GTXYT2401).

Data Availability Statement: The original contributions presented in the study are included in the article, further inquiries can be directed to the corresponding author.

Conflicts of Interest: The authors declare that they have no conflicts of interest in this work.

References

1. Lu, H.W.; Liu, L.L.; Liu, A.R.; Pi, Y.L.; Bradford, M.A.; Huang, Y.H. Effects of movement and rotation of supports on nonlinear instability of fixed shallow arches. *Thin Wall. Struct.* **2020**, *155*, 106909. [CrossRef]
2. Alneamy, A.M. Dynamic snap-through motion and chaotic attractor of electrostatic shallow arch micro-beams. *Chaos Solitons Fractals* **2024**, *182*, 114777. [CrossRef]
3. Li, Z.C.; Zheng, J.X.; Sun, Q.; He, H.T. Nonlinear structural stability performance of pressurized thin-walled FGM arches under temperature variation field. *Int. J. Non Linear Mech.* **2019**, *113*, 86–102. [CrossRef]
4. Yang, Z.C.; Liu, A.R.; Pi, Y.L.; Fu, J.Y.; Gao, Z.K. Nonlinear dynamic buckling of fixed shallow arches under impact loading: An analytical and experimental study. *J. Sound Vib.* **2020**, *487*, 115622. [CrossRef]
5. Liu, Y.Y.; Liu, A.R.; Zhang, Z.X.; Bradford, M.A.; Yang, J. Nonlinear vibration of pinned FGP-GPLRC arches under a transverse harmonic excitation: A theoretical study. *Thin Wall. Struct.* **2023**, *192*, 111099. [CrossRef]
6. Pi, Y.L.; Bradford, M.A. Nonlinear dynamic buckling of pinned–fixed shallow arches under a sudden central concentrated load. *Nonlinear Dyn.* **2013**, *73*, 1289–1306. [CrossRef]
7. Pi, Y.L.; Bradford, M.A. Multiple unstable equilibrium branches and non-linear dynamic buckling of shallow arches. *Int. J. Non-Linear Mech.* **2014**, *60*, 33–45. [CrossRef]
8. Liu, A.R.; Yang, Z.C.; Bradford, M.A.; Pi, Y.L. Nonlinear dynamic buckling of fixed shallow arches under an arbitrary step radial point load. *J. Eng. Mech.* **2018**, *144*, 04018012. [CrossRef]
9. Li, Z. Exploration of the encased nanocomposites functionally graded porous arches: Nonlinear analysis and stability behavior. *Appl. Math. Model.* **2020**, *82*, 1–16. [CrossRef]

10. Xiao, X.H.; Bu, G.B.; Ou, Z.H.; Li, Z.H. Nonlinear in-plane instability of the confined FGP arches with nanocomposites reinforcement under radially-directed uniform pressure. *Eng. Struct.* **2022**, *252*, 113670. [CrossRef]
11. Kiss, L.P. Nonlinear stability analysis of FGM shallow arches under an arbitrary concentrated radial force. *Int. J. Mech. Mater. Des.* **2020**, *16*, 91–108. [CrossRef]
12. Yan, G.; Babaei, H. Nonlinear vibration and buckling analyses of sandwich arch with titanium alloy face sheets and a porosity-dependent GPLRC core. *Acta Mech.* **2024**, *235*, 5431–5449. [CrossRef]
13. Yang, Z.C.; Barbaros, I.; Sahmani, S.; Abdussalam Nuhu, A.; Safaei, B. Size-dependent nonlinear thermomechanical in-plane stability of shallow arches at micro/nano-scale including nonlocal and couple stress tensors. *Mech. Based Des. Struct. Mach.* **2024**, *52*, 3229–3251. [CrossRef]
14. Yang, Z.C.; Liu, A.R.; Yang, J.; Lai, S.K.; Lv, J.G.; Fu, J.Y. Analytical prediction for nonlinear buckling of elastically supported fg-gplrc arches under a central point load. *Materials* **2021**, *14*, 2026. [CrossRef] [PubMed]
15. Babaei, H.; Eslami, M.R. Study on nonlinear vibrations of temperature-and size-dependent FG porous arches on elastic foundation using nonlocal strain gradient theory. *Eur. Phys. J. Plus* **2021**, *136*, 24. [CrossRef]
16. Qiao, W.Z.; Guo, T.D.; Kang, H.J.; Zhao, Y.Y. Nonlinear vibration analysis of a shallow arch coupled with an elastically constrained rigid body. *Nonlinear Dyn.* **2023**, *111*, 10769–10789. [CrossRef]
17. Zhong, Z.L.; Liu, A.R.; Fu, J.Y.; Pi, Y.L.; Deng, J.; Xie, Z.Y. Analytical and experimental studies on out-of-plane dynamic parametric instability of a circular arch under a vertical harmonic base excitation. *J. Sound Vib.* **2021**, *500*, 116011. [CrossRef]
18. Kuang, Z.X.; Liu, A.R.; Deng, J.; Fu, J.Y. Out-of-plane dynamic parametric instability of circular arches with elastic rotational restraints under a localized uniform radial periodic load. *Eng. Struct.* **2023**, *276*, 115347. [CrossRef]
19. Liu, A.R.; Lu, H.W.; Fu, J.Y.; Pi, Y.L.; Huang, Y.Q.; Li, J.; Ma, Y.W. Analytical and experimental studies on out-of-plane dynamic instability of shallow circular arch based on parametric resonance. *Nonlinear Dyn.* **2017**, *87*, 677–694. [CrossRef]
20. Zhong, Z.L.; Liu, A.R.; Pi, Y.L.; Deng, J.; Fu, J.Y.; Gao, W. In-plane dynamic instability of a shallow circular arch under a vertical-periodic uniformly distributed load along the arch axis. *Int. J. Mech. Sci.* **2021**, *189*, 105973. [CrossRef]
21. Liu, Y.Y.; Liu, A.R.; Deng, J.; Zhang, Z.X.; Wu, T.B.; Yang, J. A theoretical and experimental study on in-plane parametric resonance of laminated composite circular arches under a vertical base excitation. *Compos. Struct.* **2023**, *304*, 116398. [CrossRef]
22. Liu, Y.Y.; Liu, A.R.; Yang, J.; Zhang, Z.X.; Zhong, Z.L. In-plane dynamic instability of functionally graded porous arches reinforced by graphene platelet under a vertical base excitation. *Compos. Struct.* **2022**, *293*, 115705. [CrossRef]
23. Liu, A.R.; Yang, Z.C.; Lu, H.W.; Pi, Y.L. Experimental and analytical investigation on the in-plane dynamic instability of arches owing to parametric resonance. *J. Vib. Control* **2018**, *24*, 4419–4432. [CrossRef]
24. Zhao, S.Y.; Yang, Z.C.; Kitipornchai, S.; Yang, J. Dynamic instability of functionally graded porous arches reinforced by graphene platelets. *Thin. Wall. Struct.* **2020**, *147*, 106491. [CrossRef]
25. Ye, S.Q.; Mao, X.Y.; Ding, H.; Ji, J.C.; Chen, L.Q. Nonlinear vibrations of a slightly curved beam with nonlinear boundary conditions. *Int. J. Mech. Sci.* **2019**, *168*, 105294. [CrossRef]
26. Benedettini, F.; Alaggio, R.; Zulli, D. Nonlinear coupling and instability in the forced dynamics of a non-shallow arch: Theory and experiments. *Nonlinear Dyn.* **2012**, *68*, 505–517. [CrossRef]
27. Ouakad, H.M.; Sedighi, H.M.; Younis, M.I. One-to-one and three-to-one internal resonances in MEMS shallow arches. *J. Comput. Nonlinear Dyn.* **2017**, *12*, 051025. [CrossRef]
28. Zhou, L.Q.; Chen, Y.S.; Chen, F.Q. Global bifurcation analysis and chaos of an arch structure with parametric and forced excitation. *Mech. Res. Commun.* **2010**, *37*, 67–71. [CrossRef]
29. Yu, W.Q.; Chen, F.Q. Homoclinic orbits in a shallow arch subjected to periodic excitation. *Nonlinear Dyn.* **2014**, *78*, 713–727. [CrossRef]
30. Chtouki, A.; Lakrad, F.; Belhaq, M. Quasi-periodic bursters and chaotic dynamics in a shallow arch subject to a fast–slow parametric excitation. *Nonlinear Dyn.* **2020**, *99*, 283–298. [CrossRef]
31. Lakrad, F.; Chtouki, A.; Belhaq, M. Nonlinear vibrations of a shallow arch under a low frequency and a resonant harmonic excitations. *Meccanica* **2016**, *51*, 2577–2587. [CrossRef]
32. Hung, J.; Su, K.L.R.; Lee, Y.Y.R.; Chen, S. Various bifurcation phenomena in a nonlinear curved beam subjected to base harmonic excitation. *Int. J. Bifurc. Chaos* **2018**, *28*, 1830023. [CrossRef]
33. Bolotin, V.V. *The Dynamic Stability of Elastic Systems*, 1st ed.; Holden-Day: San Francisco, CA, USA; London, UK, 1964; pp. 324–329.
34. Zhong, Z.L.; Liu, A.R.; Guo, Y.H.; Xu, X.B.; Deng, J.; Yang, J. Sub-harmonic and simultaneous resonance instability of a thin-walled arch under a vertical base excitation at two frequencies. *Thin Wall. Struct.* **2023**, *191*, 111094. [CrossRef]
35. Shen, F.L.; Zhong, Z.L.; Xu, X.B.; Li, J.H.; Dong, Q.X.; Deng, J. In-plane simultaneous resonance instability behaviors of a fixed arch under a two-frequency radial uniformly distributed excitation. *Int. J. Non-Linear Mech.* **2025**, *174*, 105056. [CrossRef]
36. Pi, Y.L.; Trahair, N.S. Non-linear buckling and postbuckling of elastic arches. *Eng. Struct.* **1998**, *20*, 571–579. [CrossRef]

37. Emam, S.A.; Nayfeh, A.H. Non-linear response of buckled beams to 1:1 and 3:1 internal resonances. *Int. J. Non-Linear Mech.* **2013**, *52*, 12–25. [CrossRef]
38. Pi, Y.L.; Bradford, M.A.; Uy, B. In-plane stability of arches. *Int. J. Solids Struct.* **2002**, *39*, 105–125. [CrossRef]

Disclaimer/Publisher's Note: The statements, opinions and data contained in all publications are solely those of the individual author(s) and contributor(s) and not of MDPI and/or the editor(s). MDPI and/or the editor(s) disclaim responsibility for any injury to people or property resulting from any ideas, methods, instructions or products referred to in the content.